

Identification of physically consistent dynamics parameter of the ABB IRB 360-6/1600 delta robot and its use for time-optimal motion planning under consideration of constraint forces

Daniel Gnad^{a,*}, Hubert Gattringer^a, Andreas Müller^a, Wolfgang Höbarth^b, Roland Riepl^b, Lukas Meßner^b

^a Johannes Kepler University Linz, Altenberger Straße 69, Linz, 4040, Austria

^b B&R Industrial Automation GmbH, B&R Straße 1, Eggelsberg, 5142, Austria

ARTICLE INFO

Keywords:

Parallel robot
Inverse dynamics identification
Physically consistent parameter identification
Time-optimal motion planning
Constraint force

ABSTRACT

Model-based control schemes, forward dynamics simulations, constraint force computation and time-optimal motion planning have one major thing in common, they all depend on the dynamics parameters of the system. Physical consistency of the dynamics parameters ensures a positive definite mass matrix and correct constraint forces. The most common inverse dynamics identification method – the base-parameters – lack physical consistency. This paper proposes an identification method to identify physically consistent dynamics parameters for Delta-like robots while further showing the effects of friction in passive joints. A tailored model to compute the crucial constraint forces appearing in the mechanism based on the identified dynamics parameters is derived. This model is used to additionally consider constraint forces besides actuation torques for time-optimal motion planning of a typical pick and place task. This is done without any prior CAD data of the robot from the manufacturer.

1. Introduction

The equations of motion (EOM) of any robot can be expressed in the general form

$$\mathbf{M}(\mathbf{q})\ddot{\mathbf{q}} + \mathbf{C}(\mathbf{q}, \dot{\mathbf{q}})\dot{\mathbf{q}} + \mathbf{g}(\mathbf{q}) + \mathbf{f}(\mathbf{q}, \dot{\mathbf{q}}) = \boldsymbol{\tau}. \quad (1)$$

Therein, the generalized mass matrix is denoted with $\mathbf{M}(\mathbf{q})$, $\mathbf{C}(\mathbf{q}, \dot{\mathbf{q}})\dot{\mathbf{q}}$ accounts for the Coriolis and centrifugal forces, $\mathbf{g}(\mathbf{q})$ represents the potential forces and $\mathbf{f}(\mathbf{q}, \dot{\mathbf{q}})$ describes friction. The actuation forces are denoted with $\boldsymbol{\tau}$. The EOM (1) depend on the dynamics parameters \mathbf{p} and so does the generalized mass matrix $\mathbf{M}(\mathbf{q}, \mathbf{p})$. Positive definiteness of \mathbf{M} is ensured by physically consistent dynamics parameters. Positive definiteness and symmetry of the mass matrix are required for efficient forward dynamics simulations and application of various control laws [1]. According to [1] physical inconsistency of any model automatically yields instable dynamics simulation. Precise knowledge of the robot model is inevitable for model-based control schemes such as computed torque [2], passivity based control [3] or augmented PD [4], where the skew symmetry of $\frac{1}{2}\dot{\mathbf{M}} - \mathbf{C}$ is required. All these mentioned control strategies require an analytic model in the general form (1). Besides control applications, physical consistency of dynamics

parameters is crucial for constraint force computation [5,6] using an absolute coordinate model.

The most common inverse dynamics identification method are the base-parameters \mathbf{p}_B [7], which are the result of a straight forward least squares identification that does not consider physical consistency. Due to this lack the resulting generalized mass matrix $\mathbf{M}(\mathbf{p}_B, \mathbf{q})$ need not be positive definite anymore. This was noticed by [8,9] more than twenty years ago. During the last two decades, many contributions were made to achieve consistency of the dynamics parameters. The authors in [1,10] first enforced positive definiteness of the inertia tensor $\boldsymbol{\Theta}$, and [11] further incorporated the triangle inequalities, which relate the eigenvalues of the inertia tensor. Later, linear matrix inequalities (LMI) [12–15], or manifold theory [16] were introduced to address consistency. A very recent approach [17] embedded physical consistency into a non-linear parameter transformation such that unconstrained optimization methods can be applied, which eases the computational effort. So far, none of these methods have been applied to parallel robots.

Parallel robots [18], especially Delta-like manipulators, have already been subject to various inverse dynamics identifications in the literature. A *Delta-Like* manipulator [19] is understood as a (sub)category

* Corresponding author.

E-mail addresses: daniel.gnad@jku.at (D. Gnad), hubert.gattringer@jku.at (H. Gattringer), a.mueller@jku.at (A. Müller).

of a parallel kinematics machine (PKM) where each limb, connecting the moving platform with the (base) platform, comprises an actuated link followed by a parallelogram mechanism formed by two slender struts. Clavel's Delta robot [20] is the most prominent one. Further examples of Delta-Like robots are the H4 [21,22], Par2 [23], Par4 [24,25], and I4 [26]. The authors [27–34] applied the common base-parameters approach, whereas [23,35] rigorously simplified the model e.g. the struts were modeled as lumped point masses. Another inverse dynamics identification approach used Lagrange multipliers [36], or even a statistical method using a Maximum-Likelihood estimator [37] was proposed. However, none of these references considers physical consistency. For the first time in the literature, [38] proposed a method to identify a complete set of physically consistent dynamics parameters for the class of Delta-like robots. A detailed literature review on the mentioned identification methods for Delta-like robots is also provided in [38].

Constraint forces play a crucial, but mostly overlooked, role for parallel robots. Even if the actuation torques are within the set limits, constraint forces can damage or even break the mechanism if not taken into account during motion planning [39]. Delta robots are designed for highly dynamic object manipulation, which is facilitated by the lightweight structure of the mechanism. It was observed in various industrial applications that manipulation of bulky loads with Delta robots causes the mechanism to fall apart. A bulky load need not necessarily exceed the payload limit, but rather the distance from the flange or tool of the Delta robot to the center of mass (COM) of the payload causes tilting torques on the platform during object manipulation tasks. These resulting reaction forces and torques have to be compensated mainly by the strut forces of the limbs, which have been identified as a crucial force within the mechanism [39]. A major weak point of the mechanical structure are the clamped ball socket joints, as shown in Fig. 1, connecting the lightweight struts to the platform and upper arms. If the longitudinal force at the either one end of the struts exceeds a certain limit, the force created by the spring to press the socket on the ball is not sufficient anymore and the socket starts dislocating from the ball. This dislocation immediately causes the joint to fall apart. It should be remarked that some Delta robots are designed with two consecutive revolute joints instead of spherical joints. Nevertheless, many delta-like robots are designed using clamped ball-socket joints.

The contribution of this paper is an identification method to identify a complete set of physically consistent dynamics parameters for the family of Delta-like robots. The proposed identification method consists of two parts. At first the PKM is disassembled into a disconnected platform, a telescope bar, six individual struts, and the three upper arms that remain connected to the base. The inertia parameters of the disconnected parts can then be obtained. The standard base-parameter identification method [7] is applied to this system. These results are used as estimates and regularization values for physically consistent parameter identification of the assembled robot. For the latter, the non-linear parameter transformation of the dynamics parameters [38] is used to guarantee physical consistency while reducing the necessary number of optimization variables motivated by assumptions on the location of the COM and symmetry of the inertia tensor. This in turn improves the identification result. Identification of the disassembled robot in the first step reveals the effects of friction in passive joints for the assembled robot, which usually is not included in the model. The identified complete dynamics parameters for the ABB IRB 360-6/1600 are reported. Based on the identified dynamics parameters a reduced model is derived that enables computing constraint and actuation forces. In addition to the inverse dynamics verification, the model is verified against measurements of internal strut forces, which has not been reported in the literature. The reduced model considering both actuation and constraint forces is used for time-optimal motion planning and demonstrated using an optimized pick and place task.



Fig. 1. Picture of the ball socket joint and the spring clamp of the ABB IRB 360-6/1600 robot.

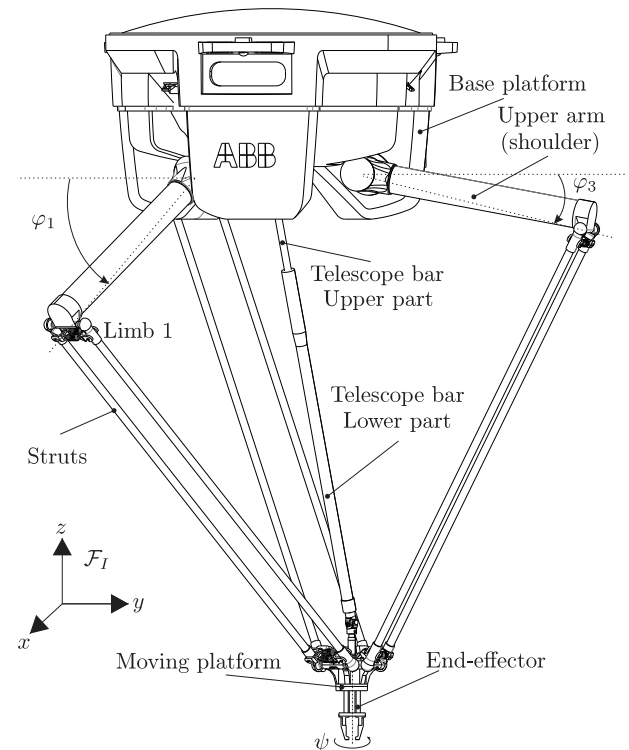


Fig. 2. Schematics of the $\delta = 4$ degree of freedom Delta robot ABB IRB 360-6/1600.

2. Model of the ABB IRB 360/1600-6 Delta

2.1. Kinematics

The Delta robot IRB 360 is shown in Fig. 2. The term Delta is used as abbreviation for Delta robot. The moving platform is connected by three limbs [40] to the base (platform). Each of the limbs consists of an actuated upper arm (also referred to as shoulder or arm) and two slender struts that form a parallelogram mechanism. The upper arms are connected by an actuated revolute joint to the base. The struts are mounted using the discussed ball socket joints to the upper arm and the platform. A telescope bar with a prismatic joint in the middle and a Cardanic suspension at both ends is used to transfer the rotation of the fourth motor to the robots end-effector (EE). Due to the two Hooke (universal or Cardan) joints that realize the Cardanic suspension the rotation of the EE ψ is equivalent to the angle of the fourth motor. The kinematics structure is visualized in Fig. 3 using a chain diagram [19].

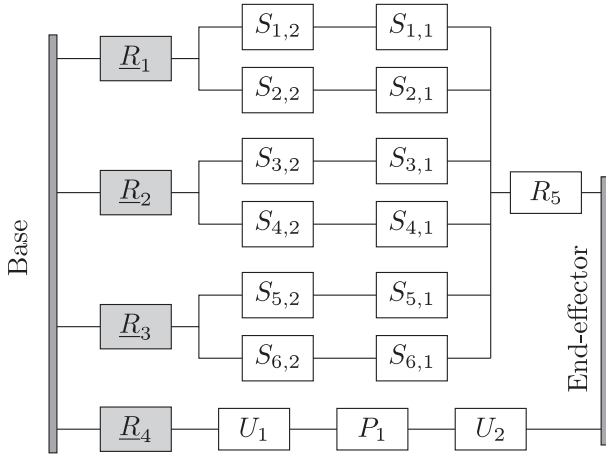


Fig. 3. Chain diagram of the Delta robot: “S” represents a spherical joint, “U” a universal joint, “R” a revolute, and “P” a prismatic joint. The underbar denotes actuation. The joints \underline{R}_i correspond to the actuated angles $\varphi_i, i = 1, \dots, 4$. The revolute joint R_5 represents the mounting of the EE to the moving platform. The rotation of the fourth motor to the EE is transferred via the joints $\underline{R}_4, U_1, P_1, U_2$.

The generalized coordinates $\mathbf{q}^T = [\varphi_1 \ \varphi_2 \ \varphi_3 \ \psi]$ are used, where $\varphi_i, i = 1, 2, 3$ denotes the angles of the three actuated upper arms and ψ the angle of the fourth motor driving the telescope bar. The angles of the upper arms and the rotation of the fourth motor are also referred to as axis in the following, e.g. axis 1 refers to φ_1 while axis 4 is used for ψ . The EE pose is expressed using the task space coordinates $\mathbf{z}^T = [\mathbf{r}^T \ \psi]$, where \mathbf{r} is the position vector to the platform resolved in the inertial frame F_I . The inverse kinematics map $\mathbf{q} = \mathbf{f}_{IK}(\mathbf{z})$ allows expressing the actuator coordinates using the task space coordinates. The frame F_A is attached at the upper arm, F_P at the moving platform, F_S at the struts, and F_{EE} at the EE (see Fig. 4). The frame at the upper part of the telescope bar is denoted with F_{TU} , and the frame F_{TL} is used for the lower part.

2.2. EOM in parameter-linear form

The inverse dynamics model establishes a relation between the robots motion and the actuation torques. This model is used for model-based control purposes, e.g. computation of feed-forward torques. The EOM are linear w.r.t. the dynamics parameters \mathbf{p} . This linearity is exploited for inverse dynamics identification of the robotic manipulator. In this section, the inverse dynamics model is briefly derived and the assumed model simplifications summarized.

Since the forward kinematics $\mathbf{z} = \mathbf{f}_{FK}(\mathbf{q})$ of the Delta robot can (locally) be solved analytically, the EOM can be written in the unconstrained form (1). This yields δ motion equations, where δ is the degree of freedom (DOF) of the manipulator. The contribution of the N moving rigid bodies of the PKM to the EOM can be rewritten in the parameter-linear form [7]

$$\mathbf{M}(\mathbf{q})\ddot{\mathbf{q}} + \mathbf{C}(\mathbf{q}, \dot{\mathbf{q}})\dot{\mathbf{q}} + \mathbf{g}(\mathbf{q}) = \sum_{i=1}^N \mathbf{Y}_i(\mathbf{q}, \dot{\mathbf{q}}, \ddot{\mathbf{q}}) \mathbf{p}_i \quad (2)$$

with the $\delta \times 10$ regressor matrices \mathbf{Y}_i and inertia parameter vectors

$$\mathbf{p}_i^T = [m \quad m\mathbf{c}^T \quad \theta_{xx} \quad \theta_{yy} \quad \theta_{zz} \quad \theta_{xy} \quad \theta_{yz} \quad \theta_{xz}] \quad (3)$$

of each rigid body i . The inertia parameter vector \mathbf{p} comprises the mass m , the first mass moment $m\mathbf{c}$ with the position vector \mathbf{c} from the joint frame to the COM, and the second moments of the symmetric inertia tensor

$$\boldsymbol{\theta} = \begin{bmatrix} \theta_{xx} & \theta_{xy} & \theta_{xz} \\ \theta_{xy} & \theta_{yy} & \theta_{yz} \\ \theta_{xz} & \theta_{yz} & \theta_{zz} \end{bmatrix} \quad (4)$$

w.r.t. the joint (or link) frame.

Viscous and Coulomb friction are modeled for the actuated joints. In case of the IRB 360, the prismatic joint of the telescope bar shows non-negligible friction that is also considered. Friction occurring in n_f joints is represented by

$$\mathbf{f}(\mathbf{q}, \dot{\mathbf{q}}) = \mathbf{Y}_f(\mathbf{q}, \dot{\mathbf{q}}) \mathbf{p}_f = \mathbf{Y}_v \mathbf{p}_v + \mathbf{Y}_c \mathbf{p}_c \quad (5)$$

which splits into viscous friction $\mathbf{Y}_v \mathbf{p}_v$, and Coulomb friction $\mathbf{Y}_c \mathbf{p}_c$. Viscous friction models for the velocity dependent friction, whereas Coulomb friction accounts for the static friction during any motion. For more details on various friction models the reader is referred to the rich literature on this topic. The viscous friction parameter vector $\mathbf{p}_v^T = [p_{v1} \ \dots \ p_{v n_f}]$ and Coulomb friction coefficients $\mathbf{p}_c = [p_{c1} \ \dots \ p_{c n_f}]$ are comprised by the friction coefficient vector $\mathbf{p}_f^T = [\mathbf{p}_v^T \ \mathbf{p}_c^T]$. The resulting $\delta \times 2n_f$ matrix $\mathbf{Y}_f = [\mathbf{Y}_v \ \mathbf{Y}_c]$ contains the $\delta \times n_f$ regressor matrices \mathbf{Y}_v and \mathbf{Y}_c . The viscous friction regressor matrix

$$\mathbf{Y}_v = \begin{bmatrix} \text{diag}(\dot{\mathbf{q}}) & \left(\delta_i \frac{\partial \dot{\theta}_i}{\partial \dot{\mathbf{q}}} \right)_{i=1 \dots n_f - \delta}^T \end{bmatrix} \quad (6)$$

consists of a diagonal matrix of the actuated joint velocities $\text{diag}(\dot{\mathbf{q}})$ and partial derivatives of velocities $\dot{\theta}_1, \dots, \dot{\theta}_{n_f - \delta}$ of further joints whose friction is modeled [41]. The linear velocity along the axis of the telescope bar is considered as such a further velocity. Throughout the paper $\text{diag}(\mathbf{x}) = \text{diag}(x_1, \dots, x_n)$ for $\mathbf{x} \in \mathbb{R}^n$ is used to denote a diagonal matrix with the elements of a vector. Coulomb (or static) friction is expressed by the regressor matrix

$$\mathbf{Y}_c = \begin{bmatrix} \text{diag}(\text{sign}(\dot{\mathbf{q}})) & \left(\text{sign}(\dot{\theta}_j) \frac{\partial \dot{\theta}_j}{\partial \dot{\mathbf{q}}} \right)_{j=1 \dots n_f - \delta}^T \end{bmatrix}, \quad (7)$$

where sign denotes the sign function. In the following the $\tanh(\cdot)$ function is used as continuous approximation of the discontinuous $\text{sign}(\cdot)$ function. The advantage of the $\tanh(\cdot)$ function is the continuity when the argument is close to zero.

The $10N$ inertia and $2n_f$ friction parameters are summarized in the parameter vector $\mathbf{p}^T = [\mathbf{p}_1^T \ \dots \ \mathbf{p}_N^T \ \mathbf{p}_f^T]$ such that

$$\boldsymbol{\tau} = \mathbf{Y}(\mathbf{q}, \dot{\mathbf{q}}, \ddot{\mathbf{q}}) \mathbf{p}. \quad (8)$$

2.3. Model assumptions for the Delta robot

2.3.1. Rigid body parameters

The proposed model simplifications for the ABB IRB 360-6/1600 are discussed in detail in [38] and are briefly summarized in the following. This allows to systematically reduce the required number of optimization variables.

Deviation moments. It is common practice to omit the deviation moments of the inertia tensor $\theta_{xy}, \theta_{yz}, \theta_{xz}$ since the considered joint frames are usually assumed to be aligned with the principal axis frame of the respective body.

Upper arms. The upper arms perform only a one dimensional rotatory motion, hence the only excited parameters are the first moments $m c_x$ and $m c_z$ as well as the inertia entry θ_{yy} , all expressed w.r.t. the joint frame F_A in Fig. 4. This still yields the exact EOM for the upper arms.

Struts. The COM of the slender struts is assumed in the geometric center along the center line in x direction resolved in the joint frame F_S , as shown in Fig. 4. This implies that the first mass moments $m c_y = m c_z = 0$. Assuming symmetry such that $\theta_{yy} = \theta_{zz}$ further reduces the number of parameters to be identified.

Platform. The platform of the Delta robot can only perform translational motions, hence it is sufficient to only consider the mass m of the platform. The mass moments $m\mathbf{c}$ and $\boldsymbol{\theta}$ do not contribute to the EOM (1) and cannot be identified.

However, for the in Section 4 discussed computation of constraint forces the location of the COM of the platform is required and assumed

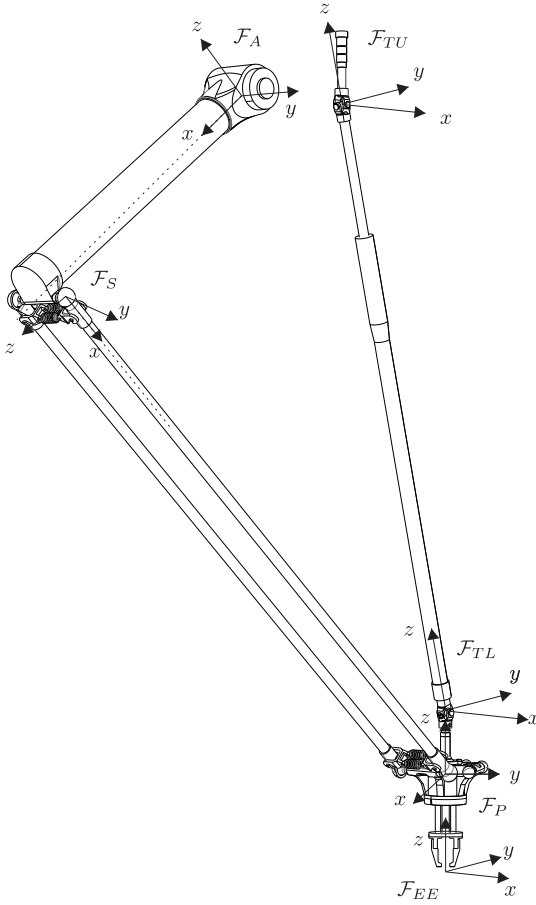


Fig. 4. Detailed view of the first limb and the telescope bar with the corresponding joint frames.

to be located at the center line of the platform and 20 mm below the plane created by centers of the six spherical joints. This assumption is derived from a simplified CAD model of the platform. The CAD model from the manufacturer does not contain closed surfaces or information about the density and is hence insufficient.

Telescope bar. The two parts of the telescope bar are simplified analogously to the struts. The COM is assumed to be on the center line along the z axis of frame F_{TU} for the upper and F_{TL} for the lower part, as shown in Fig. 4. This assumption yields $m_{c_x} = m_{c_y} = 0$ for the first lateral mass moments for both parts. Again, assuming symmetry such that $\Theta_{xx} = \Theta_{yy}$ for both parts is a further simplification.

End-effector. The tool mounted on the EE can be assumed well known, such that a valid set of inertia parameters is available. However, if the EE tool has to be identified, the executable motions of the EE define the identifiable inertia parameters. The EE performs the translational motion predetermined by the platform together with the rotation transferred via the telescope bar. Due to the kinematics only the mass m , first mass moments m_{c_x}, m_{c_y} and the rotatory inertia Θ_{zz} contribute to the EOM.

2.3.2. Exploiting the parallel structure

The special structure of the Delta PKM is further exploited assuming that each of the limbs is represented by the same parameter set. Justified by the results in Section 6.2.2, where the upper arms are treated as different rigid bodies, only one parameter set for each limb will be modeled in Section 6.3.3. This assumption further increases the contribution of these parameters to the actuation torques τ and hence

their identifiability. A major benefit of assuming identical rigid bodies is the drastic reduction of unknown parameters to be estimated.

As an example, consider Clavel's original Delta. It consists of three identical limbs, each one containing three bodies, this yields 90 inertia parameters and together with the platform amounts to 100 parameters. Assuming that all limbs are identically manufactured, reduces the 90 parameters to 20 and the complete system to 30. This results in a reduction of 70% of the unknown parameters!

3. Identification procedure

The proposed identification procedure consists of two parts. First, the standard base-parameter identification method is applied to the disassembled system consisting of three upper arms. In this case the base-parameters are the complete set of parameters needed in the EOM. The inertia parameter of the platform struts, and telescope bar are identified separately. In the second step a complete set of physically consistent parameters of the assembled PKM is identified using the results of the first step.

3.1. Determination of base-parameters

The regressor matrix $Y(\mathbf{q}, \dot{\mathbf{q}}, \ddot{\mathbf{q}})$ is rank deficient [7]. Numerical decomposition methods like a QR factorization or singular value decomposition (SVD) are used to determine the n_B independent columns of the regressor matrix Y . These n_B independent columns form the full rank base-parameter regressor matrix Y_B . The reduction of the columns further yields the identifiable minimal set of base-parameters \mathbf{p}_B , which are a linear combination of the complete set of dynamics parameters \mathbf{p} . The base-parameter regressor matrix Y_B and parameter vector \mathbf{p}_B are used for the inverse dynamics model $\tau = Y_B \mathbf{p}_B$. The reader is referred to [7] for a more detailed explanation and derivation. It should be mentioned that the QR factorization is not unique, nor is the set of base-parameters. The reduced regressor matrix Y_B is required for the optimization of persistent excitation trajectories [42].

For the identification, the persistent excitation trajectory is executed and the joint angles \mathbf{q} and torques τ are recorded. The joint velocities $\dot{\mathbf{q}}$ and accelerations $\ddot{\mathbf{q}}$ are computed using numerical differentiation. For each measurement the full rank regressor matrix Y_B and actuation torque vector τ are evaluated. The so obtained matrices and vectors are stacked to form a matrix \bar{Y}_B and vector $\bar{\tau}$, respectively. The base-parameter vector \mathbf{p}_B is the unique solution to the regression problem $\min_{\mathbf{p}_B} \|\bar{\tau} - \bar{Y}_B \mathbf{p}_B\|_{W_\tau}^2$, where $\|\mathbf{x}\|_W = \sqrt{\mathbf{x}^T W \mathbf{x}}$ denotes the weighted norm of vector \mathbf{x} . The base-parameter vector is thus obtained as

$$\mathbf{p}_B = (\bar{Y}_B^T W_\tau \bar{Y}_B)^{-1} \bar{Y}_B^T W_\tau \bar{\tau}. \quad (9)$$

If the inverse covariance matrix Σ^{-1} of the torque measurement is used as weighting matrix W_τ then the result is the minimum variance, unbiased (MVU) Gauss–Markov estimator [43,44]. However, for application of the MVU estimator, an estimate of the covariance matrix of the torque measurement is needed [45]. An alternative to the covariance matrix Σ is to use the weighting matrix $W_\tau = \text{diag}(\tau_i)^{-2}$ constructed from the maximal actuation torques τ_i . This makes the error dimensionless and further scales the influence of axes with less nominal/maximal torque (as it is with the fourth axis of the Delta) to the cost function.

3.2. Identification of complete parameters of the assembled PKM

A persistent excitation trajectory [46–48] is executed and recorded yielding n_s (time) samples of the joint angles \mathbf{q} and motor torques τ . For a PKM it is preferable to parameterize the EE motion [32–34,37,38] rather than the joint angles using a (truncated) Fourier series. Restricting the EE motion to stay within the admissible task space, or an approximation as shown in Fig. 5, eliminates the need for a collision avoidance for the computation of the excitation trajectory.

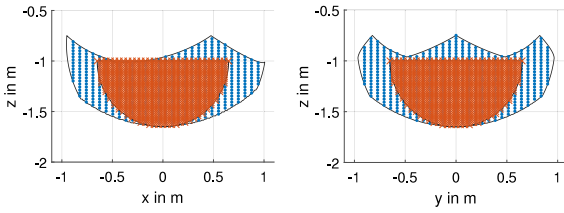


Fig. 5. Approximation of the task space (blue dotted texture) of the IRB 360 using a hemisphere (orange and more dense pattern). The limited length of the telescope bar is the most restrictive joint constraint for the task space. (For interpretation of the references to color in this figure legend, the reader is referred to the web version of this article.)

The regressor matrix $\mathbf{Y}(\mathbf{q}, \dot{\mathbf{q}}, \ddot{\mathbf{q}})$ and the actuation torque vector $\boldsymbol{\tau}$ are evaluated and stacked to obtain the $\delta n_s \times (10N + 2n_f)$ matrix $\bar{\mathbf{Y}}$ and the δn_s vector $\bar{\boldsymbol{\tau}}$. The identification problem boils down to minimizing the weighted, squared error $\|\bar{\boldsymbol{\tau}} - \bar{\mathbf{Y}}\mathbf{p}\|_{\mathbf{W}_\tau}^2$, where again $\mathbf{W}_\tau = \text{diag}(\tau_i)^{-2}$ is used to normalize and homogenize the error. Since the regressor matrix is inherently rank deficient [7], there is no unique solution. The unique solution minimizing the error is given in (9). In order to obtain parameters that are in correspondence with estimated parameters or available from data sheet parameters, regularization values \mathbf{p}_{reg} are prescribed and the objective function

$$J(\mathbf{p}) := \frac{\gamma_\tau}{n_s} \|\bar{\boldsymbol{\tau}} - \bar{\mathbf{Y}}\mathbf{p}\|_{\mathbf{W}_\tau}^2 + \sum_{i=1}^N \gamma_{\text{reg},j} d(\mathbf{p}_i, \mathbf{p}_{\text{reg},i}) + \gamma_{\text{reg},f} \|\mathbf{p}_f - \mathbf{p}_{\text{reg},f}\|_{\mathbf{W}_p}^2 \quad (10)$$

is minimized. The scalar factor γ_τ is introduced to weigh the effect of the torque error in the cost function. The distance measure $d(\mathbf{p}(\boldsymbol{\pi}), \mathbf{p}_{\text{reg}})$ is used to compare two different parameter vectors. In [15,16] a matrix norm $d(\bar{\mathbf{M}}(\mathbf{p}), \bar{\mathbf{M}}(\mathbf{p}_{\text{reg}}))$ was used instead of a vector norm. In the following, the relative error

$$d(\mathbf{p}, \mathbf{p}_{\text{reg}}) = \|\mathbf{p} - \mathbf{p}_{\text{reg}}\|_{\mathbf{W}_p}^2 \quad (11)$$

with $\mathbf{W}_p = \text{diag}(\mathbf{p}_{\text{reg}})^{-2}$ is used since it offers an intuitive and interpretable comparison of inertia parameters. The ratio $\gamma_\tau/\gamma_{\text{reg}}$ of the scalar tuning factors determines how close the obtained result is to the used regularization value. The smaller the ratio is, the closer the result will be to the regularization value. The coefficients $\gamma_{\text{reg},j}$ accounts for the regularization of the inertia parameters, whereas $\gamma_{\text{reg},f}$ refers to the friction coefficients. Based on the trustworthiness of the regularization values these coefficients can differ. Hence, they are separately stated in (10).

To minimize (10) without imposing LMI constraints the non-linear parameter transformation derived in [17] and further simplified in [38] is used. This transformation $\mathbf{p}(\boldsymbol{\pi})$ uses an algorithmic set of parameters $\boldsymbol{\pi}$ that describe a deformation of a reference body, which in turn preserves consistency. Hence, the parameters $\boldsymbol{\pi}$ are the optimization variables for the identification procedure to guarantee physically consistent dynamics parameters. For a detailed explanation of the non-linear parameter transformation dedicated to identifying Delta-like robots the reader is referred to [38]. In [38] the systematic reduction of the optimization variables $\boldsymbol{\pi}$ based on geometric assumptions is derived. The non-linear parameter transformation is preferred over the LMI approaches since it boils down to an unconstrained optimization problem.

3.3. Remaining regularization values

The regularization values \mathbf{p}_{reg} ensure a unique minimum of the cost function (10) and further serve as initial values for the identification procedure. However, useful CAD parameters are rarely provided by

robot manufacturers. The outer geometry can easily be measured, whereas approximating the mass is the challenging part due to the unknown density. Nevertheless, disassembling the PKM and actually measuring the mass of the struts, platform, and telescope bar of the Delta is a convenient approach to obtain very good regularization values. The links/bodies of the Delta robot are approximated by cylindrical objects. The formulae $\frac{1}{2}mR^2$ and $\frac{1}{12}m(L^2 + 3R^2)$ for a cylinder, or $\frac{1}{2}m(r^2 + R^2)$ and $\frac{1}{12}m(L^2 + 3(r^2 + R^2))$ for a hollow cylinder, where m denotes the mass, L the length, r the inner radius, and R the outer radius, are used to compute the inertia w.r.t. to the COM. Application of the parallel axis theorem using the assumed position of the COM provides a practical approach to compute the required regularization values.

Removing the platform, struts and telescope bar from the mechanism reduces the three limbs and just the upper arms and the fourth motor remain. The kinematic loops are opened since the linkages are not connected anymore. Identification of this simple system(s) in an intermediate step yields regularization values for the upper arms and occurring friction in the drives. This strategy is not applicable for serial manipulators, since they cannot easily be disassembled with every active joint being still fully functional.

4. Computation of constraint forces

The classical method to compute constraint forces is by means of an absolute coordinate model and the use of Lagrange multipliers. This requires all 10 inertia parameters of every rigid body of the robot. On the other hand, for computing only certain constraint forces (e.g. longitudinal strut forces) a reduced model with less complexity than the absolute coordinate model is introduced.

The kinematics are modeled completely, and the closed form solution ensures accurate motion of the robot. The kinematics solution is used to compute the twist $\mathbf{V}^T = [\mathbf{v}^T \ \boldsymbol{\omega}^T]$ comprising the translational (linear) velocity \mathbf{v} and angular velocity $\boldsymbol{\omega}$ of each of the rigid bodies. A joint connecting two adjacent bodies puts constraints on their twists. Depending on the joint, the twists are related by velocity constraint Jacobian [5,6]. A reduced system of constraints is introduced that reveal the constraint reaction forces/torques that are of interest, e.g. for motion planning. These reduced constraints would not be sufficient for a correct kinematic modeling. Furthermore, the servo constraints [49] are considered to account for the necessary actuation of the desired motion. In this case, the Lagrange multipliers λ comprise the selected constraint forces due to the joints and the related actuation torques.

The prismatic joint of the telescope bar connecting the upper and lower part allows for free unconstrained motion along the longitudinal direction. For simplicity, the telescope bar is omitted, but the weight of the lower part of the telescope bar is added to the platform to still account for the moving mass of the lower part. The lateral forces appearing at the spherical joints of the platform are omitted and only the crucial longitudinal forces along the struts are considered. As shown in [39], the lateral forces are within ± 1 N, whereas the longitudinal forces reach values of ± 120 N and more if not limited. The analytic solution of the kinematics of the mechanism (Section 2.1) is used to compute the feasible twists \mathbf{V} and accelerations $\dot{\mathbf{V}}$, as explained in the following. Using the analytic solution of the kinematics of the mechanism, the resulting motion equations represent an algebraic equation system for the Lagrange multipliers λ rather than a differential algebraic equation system for λ and $\dot{\mathbf{V}}$. The following motion equations are expressed w.r.t. the COM, but for the upper arms the equations are expressed in the link frame.

4.1. Revolute joint R_5 between end-effector and platform

The EE of the Delta performs a translation due to the platform motion and the rotation due to the telescope bar. The EE is connected

with a revolute joint to the platform. The corresponding five velocity constraints on the EE twist \mathbf{V}_E and platform twist \mathbf{V}_P are

$$[\mathbf{G}_E \quad \mathbf{G}_{P,1}] \begin{bmatrix} \mathbf{V}_E \\ \mathbf{V}_P \end{bmatrix} = \mathbf{0}. \quad (12)$$

The analytic kinematics solution is used to directly compute the allowed twists

$$\mathbf{V}_E = \begin{bmatrix} \mathbf{v}_E \\ \omega_E \end{bmatrix} = \begin{bmatrix} \mathbf{v}_E \\ 0 \\ 0 \\ \omega_z \end{bmatrix}, \mathbf{V}_P = \begin{bmatrix} \mathbf{v}_P \\ \omega_P \end{bmatrix} = \begin{bmatrix} \mathbf{v}_P \\ 0 \\ 0 \\ 0 \end{bmatrix} \quad (13)$$

resolved in the frames \mathcal{F}_E and \mathcal{F}_P , respectively.

This yields five Newton–Euler (NE) equations for the EE

$$\begin{bmatrix} \mathbf{I}_5 & \mathbf{0} \end{bmatrix} (\mathbf{M}_E \dot{\mathbf{V}}_E + \mathbf{C}_E \mathbf{M}_E \mathbf{V}_E + \mathbf{G}_E^T \lambda_E) = \begin{bmatrix} \mathbf{I}_5 & \mathbf{0} \end{bmatrix} \mathbf{W}_E \quad (14)$$

expressed in the COM and the body fixed reference frame of the EE. The subscript of the identity matrix denotes its dimension to improve readability. Therein, \mathbf{M}_E denotes the 6×6 inertia matrix, $\mathbf{C}_E = \text{blkdiag}(\tilde{\omega}, \tilde{\omega})$ is used to represent the Coriolis and centrifugal terms $\mathbf{C}_E \mathbf{M}_E \mathbf{V}_E$, where $\tilde{\omega}$ is the skew symmetric matrix associated to ω , and \mathbf{W}_E is the gravitation wrench. Throughout the paper, $\text{blkdiag}(\mathbf{A}_1, \mathbf{A}_2)$ is used to express the block diagonal matrix of the matrices $\mathbf{A}_1, \mathbf{A}_2$. The vector $\lambda_E^T = [\lambda_{E,1} \quad \dots \quad \lambda_{E,5}]$ of Lagrange multipliers comprises the three constraint forces and two constraint torques in the 1-DOF revolute joint R_5 .

The advantage of using the complete kinematics solution becomes visible when taking a closer look at the momentum of the EE $\Pi_E = \mathbf{M}_E \mathbf{V}_E$ expressed in the COM

$$\Pi_E = \begin{bmatrix} m_E \mathbf{I} & \mathbf{0} \\ \mathbf{0} & \boldsymbol{\Theta}_E \end{bmatrix} \begin{bmatrix} \mathbf{v}_E \\ \omega_E \end{bmatrix} = \begin{bmatrix} m_E \mathbf{v}_E \\ 0 \\ 0 \\ \Theta_{zz} \omega_z \end{bmatrix}. \quad (15)$$

Expressing the NE in the COM lets the coupling terms (off diagonal entries) of the inertia matrix vanish. Using the feasible twist for the EE derived from the complete kinematics solution shows that the inertia moments Θ_{xx}, Θ_{yy} of the EE need not be available.

4.2. Spherical joints $S_{i,1}$ between platform and struts

Since only the longitudinal strut forces are of interest, the constraints for the spherical joint (connecting the lower end of the strut and the platform) are adapted. The constraint enforces the distance of the platform along the strut only. For each of the $i = 1 \dots 6$ struts a scalar valued constraint of the form

$$\mathbf{e}_{S_i}^T [\mathbf{G}_{P,2} \quad \mathbf{G}_{S,1}] \begin{bmatrix} \mathbf{V}_P \\ \mathbf{V}_S \end{bmatrix} = 0 \quad (16)$$

is introduced. Therein, \mathbf{e}_{S_i} is the unit vector along strut i , \mathbf{v}_{S_i} is the corresponding three dimensional translational velocity of strut i , and \mathbf{V}_P is the platform twist as in (13). These 6 scalar valued constraint equations

$$\begin{bmatrix} \mathbf{e}_{S_1}^T \mathbf{G}_{P,2} & \mathbf{e}_{S_1}^T \mathbf{G}_{S,1} & & & & \\ \vdots & & & & & \\ \mathbf{e}_{S_6}^T \mathbf{G}_{P,2} & & & \mathbf{e}_{S_6}^T \mathbf{G}_{S,1,6} & & \end{bmatrix} \begin{bmatrix} \mathbf{V}_P \\ \mathbf{V}_{S_1} \\ \vdots \\ \mathbf{V}_{S_6} \end{bmatrix} = \mathbf{0} \quad (17)$$

are summarized as

$$[\tilde{\mathbf{G}}_{P,2} \quad \tilde{\mathbf{G}}_{S,1}] \begin{bmatrix} \mathbf{V}_P \\ \tilde{\mathbf{V}}_S \end{bmatrix} = \mathbf{0}. \quad (18)$$

Each of the constraints in (18) accounts for the longitudinal velocity v_{S,i_x} of the struts. To this end, the longitudinal velocities of the six struts are collected in $\tilde{\mathbf{V}}_S^T = [v_{S,1_x} \quad \dots \quad v_{S,6_x}]$. The subscript $(\cdot)_x$ is used to

indicate this since the x -axis of frame \mathcal{F}_S points along the longitudinal axis of the struts.

The six NE equations for the platform are

$$\mathbf{M}_P \dot{\mathbf{V}}_P + \mathbf{G}_{P,1}^T \lambda_E + \tilde{\mathbf{G}}_{P,2}^T \lambda_P = \mathbf{W}_P, \quad (19)$$

where the Coriolis and centrifugal forces $\mathbf{C}_P \mathbf{M}_P \mathbf{V}_P$ vanish since the platform can only perform translational motions and the NE equations are w.r.t. the COM frame. The Lagrange multipliers $\lambda_P^T = [\lambda_{P,1} \quad \dots \quad \lambda_{P,6}]$ represents the six longitudinal forces in the struts at the lower end acting on the platform. Similar to (14), the NE equations of the platform are stated w.r.t. the COM, see Section 2.3. The momentum of the platform

$$\Pi_P = \mathbf{M}_P \mathbf{V}_P = \begin{bmatrix} m_P \mathbf{I} & \mathbf{0} \\ \mathbf{0} & \boldsymbol{\Theta}_P \end{bmatrix} \begin{bmatrix} \mathbf{v}_P \\ \mathbf{0} \end{bmatrix} = \begin{bmatrix} m_P \mathbf{v}_P \\ \mathbf{0} \end{bmatrix} \quad (20)$$

using the kinematics solution for the platform twist \mathbf{V}_P shows that the inertia tensor $\boldsymbol{\Theta}_P$ is not needed and only the mass of the platform m_P occurs in (19).

4.3. Spherical joints $S_{i,2}$ between struts and upper arm

The longitudinal force of the struts is crucial, as discussed in Section 1. Analogously to (16), the velocity constraint of the spherical joint connecting a strut to an arm

$$\mathbf{e}_1^T [\mathbf{G}_{S,2i} \quad \mathbf{G}_{A_j}] \begin{bmatrix} \mathbf{v}_{S_i} \\ \omega_{A_j} \end{bmatrix} = 0 \quad (21)$$

is adapted, where ω_{A_j} denotes the angular velocity of upper arm $j = 1 \dots 3$. The velocity constraint of the ball joint is projected in the longitudinal direction of the strut, represented by $\mathbf{e}_1^T = [1 \quad 0 \quad 0]$ resolved in the frame \mathcal{F}_S of strut i . These six constraints are collected in

$$[\tilde{\mathbf{G}}_{S,2} \quad \tilde{\mathbf{G}}_A] \begin{bmatrix} \tilde{\mathbf{V}}_S \\ \tilde{\mathbf{V}}_A \end{bmatrix} = \mathbf{0} \quad (22)$$

using $\tilde{\mathbf{V}}_A^T = [\omega_{A_1} \quad \dots \quad \omega_{A_3}]$, where ω_{A_j} is the y angular velocity expressed in the joint frames \mathcal{F}_A of arm j .

For each of the six struts the linear momentum balance in longitudinal direction

$$\mathbf{e}_1^T (m_S \dot{\mathbf{V}}_S + \tilde{\mathbf{m}}_S \mathbf{V}_S + \mathbf{G}_{S,1i}^T \lambda_{P,i} + \mathbf{G}_{S,2i}^T \lambda_{S,i}) = \mathbf{e}_1^T \mathbf{f}_{\text{grav}} \quad (23)$$

w.r.t. the COM is derived. The only required parameter is the identifiable mass m_S of the struts. The gravitation force is accounted for by \mathbf{f}_{grav} . The six scalar equations of the struts are summarized as

$$\tilde{\mathbf{M}}_S \dot{\tilde{\mathbf{V}}}_S + \tilde{\mathbf{C}}_S \tilde{\mathbf{M}}_S \tilde{\mathbf{V}}_S + \tilde{\mathbf{G}}_{S,1}^T \lambda_P + \tilde{\mathbf{G}}_{S,2}^T \lambda_S = \tilde{\mathbf{W}}_S. \quad (24)$$

The matrix $\tilde{\mathbf{M}}_S = m_S \mathbf{I}$ is defined by the mass of the struts, which is assumed to be identical for all 6 struts. The contribution of the Coriolis and centrifugal parts for each of the struts is accounted for by $\tilde{\mathbf{C}}_S \tilde{\mathbf{M}}_S \tilde{\mathbf{V}}_S$ and the partial contribution of the gravitation is denoted by $\tilde{\mathbf{W}}_S$. The Lagrange multipliers $\lambda_S^T = [\lambda_{S,1} \quad \dots \quad \lambda_{S,6}]$ comprise the six longitudinal forces in the struts acting between the upper end of the struts and the arms.

4.4. Servo constraints

4.4.1. Revolute joint R_i between upper arms and base

The upper arms are connected by three rugged revolute joints $R_i, i = 1, 2, 3$ to the base. The joint reaction forces and torques of these sturdy joints are not of interest given the dimension compared to the other joints in the robot.

To obtain the three motor torques acting on the upper arms the three servo constraints

$$\mathbf{e}_5^T \mathbf{V}_{A,j} = \dot{\varphi}_j \quad (25)$$

are introduced with $\mathbf{e}_5^T = [0 \ 0 \ 0 \ 0 \ 1 \ 0]$. The corresponding constraints are

$$\mathbf{e}_5^T (\mathbf{M}_A \dot{\mathbf{V}}_A + \mathbf{C}_A \mathbf{M}_A \mathbf{V}_A + \bar{\mathbf{G}}_A^T \lambda_S + \mathbf{e}_5 \lambda_A) = \mathbf{e}_5^T \mathbf{W}_A. \quad (26)$$

Using the available kinematics solution of the arms the momentum reduces to

$$\Pi_A = \begin{bmatrix} m_A \mathbf{I} & m\tilde{\mathbf{c}} \\ m\tilde{\mathbf{c}} & \Theta \end{bmatrix} \begin{bmatrix} \mathbf{0} \\ \omega_y \\ 0 \end{bmatrix} = \begin{bmatrix} -m c_z \omega_y \\ 0 \\ m c_z \omega_y \\ 0 \\ \Theta_{yy} \omega_y \\ 0 \end{bmatrix} \quad (27)$$

expressed w.r.t. to the link frame \mathcal{F}_A . The only required parameters are the identifiable inertia Θ_{yy} and the mass moment $m c_z$.

The three resulting scalar equations for the upper arms are summarized as

$$\bar{\mathbf{M}}_A \dot{\mathbf{V}}_A + \bar{\mathbf{G}}_A^T \lambda_S + \lambda_A = \bar{\mathbf{W}}_A. \quad (28)$$

The Lagrange multipliers λ_A account for the necessary actuation torques acting on the upper arms needed to perform the prescribed motion.

4.4.2. Revolute joint R_5 between EE and telescope bar

The constraint forces appearing in the actuated revolute joint R_1 , the two universal joints U_1, U_2 and the prismatic joint P_1 of the telescope bar are not of interest. The occurring constraint forces are negligible, only the required actuation for the rotation of the EE is to be considered.

The actuation of the EE via the telescope bar is expressed by the servo constraint

$$\mathbf{e}_6^T \mathbf{V}_E = \dot{\psi}(t) \quad (29)$$

with $\mathbf{e}_6^T = [0 \ 0 \ 0 \ 0 \ 0 \ 1]$. This yields the sixth NE equation for the EE as

$$\mathbf{e}_6^T (\mathbf{M}_E \dot{\mathbf{V}}_E + \mathbf{C}_E \mathbf{M}_E \mathbf{V}_E + \mathbf{G}_E^T \lambda_E + \mathbf{e}_6 \lambda_{TB}) = \mathbf{e}_6^T \mathbf{W}_E, \quad (30)$$

where λ_{TB} accounts for the necessary torque for the prescribed rotation of the EE.

4.5. Overall EOM system

The motion Eqs. (14), (19), (24), (28), (30) are summarized in

$$\mathbf{M} \dot{\mathbf{V}} + \mathbf{C} \mathbf{M} \mathbf{V} + \mathbf{G}^T \lambda = \mathbf{W}, \quad (31)$$

with $\mathbf{M} = \text{blkdiag}(\mathbf{M}_E, \mathbf{M}_P, \bar{\mathbf{M}}_S, \bar{\mathbf{M}}_A)$, the collection of twists and reduced velocities $\mathbf{V}^T = [\mathbf{V}_E^T \ \mathbf{V}_P^T \ \bar{\mathbf{V}}_S^T \ \bar{\mathbf{V}}_A^T]$ together with their corresponding Coriolis and centrifugal terms denoted with $\mathbf{C} = \text{blkdiag}(\mathbf{C}_E, \mathbf{0}, \bar{\mathbf{C}}_S, \mathbf{0})$. The (reduced) gravity wrenches are summarized in $\mathbf{W}^T = [\mathbf{W}_E^T \ \mathbf{W}_P^T \ \bar{\mathbf{W}}_S^T \ \bar{\mathbf{W}}_A^T]$. The overall 21×21 constraint Jacobian is

$$\mathbf{G} = \begin{bmatrix} \mathbf{G}_E & \mathbf{G}_{P,1} & & \\ \mathbf{e}_6^T & & & \\ & \bar{\mathbf{G}}_{P,2} & \bar{\mathbf{G}}_{S,1} & \\ & & \bar{\mathbf{G}}_{S,2} & \bar{\mathbf{G}}_A \\ & & & \mathbf{I} \end{bmatrix}, \quad \lambda = \begin{bmatrix} \lambda_E \\ \lambda_{TB} \\ \lambda_P \\ \lambda_S \\ \lambda_A \end{bmatrix}, \quad (32)$$

which accounts for the reduced joint constraints and the servo constraints.

The motion of the robot is completely described by the EE motion $\dot{\mathbf{V}}$. Because \mathbf{G} is a regular 21×21 matrix, for given $\mathbf{V}, \dot{\mathbf{V}}$ (31) is a linear equation system for λ . The topology of the regular 21×21 velocity constraint Jacobian \mathbf{G} can be exploited to efficiently solve (31) for λ by means of a block Gaussian elimination procedure. Fig. 6 graphically summarizes the computed constraint forces. The presented approach

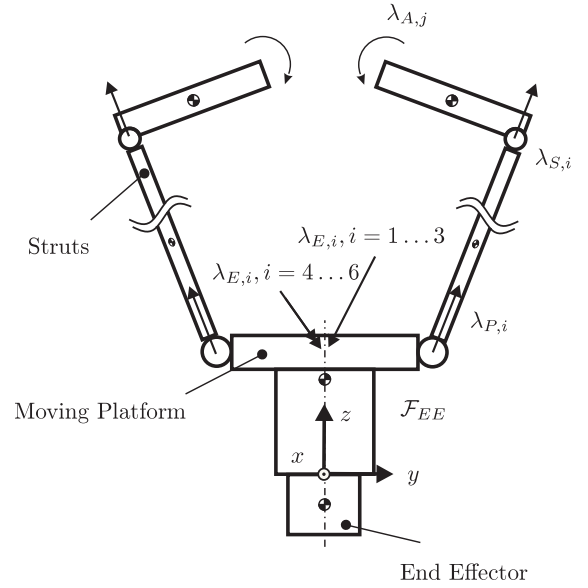


Fig. 6. Schematics of the EE, platform, struts and upper arms of the Delta robot for the constraint force computation. The flange is part of the platform.

generally applies to a system with kinematic topology of Delta-like robots.

The model (31) for the Delta robot IRB 360 accounts for the relevant constraint forces. The longitudinal strut forces are important forces to be accounted for during motion planning. The absolute coordinate model of the Delta robot derived in [39] that accounts for all constraint forces requires more dynamics parameters than are identifiable. However, not all constraint forces are necessary. This motivates the derivation of the reduced model parameterized by the identifiable parameters. Furthermore, this yields a drastic computational benefit when comparing the resulting equation system for the reduced as well as the absolute coordinate model. For the reduced model (31) the constraint Jacobian \mathbf{G} has dimension 21×21 , whereas the *extended constraint Jacobian* \mathbf{G}_{ext} in [39] has dimension 82×82 . The structure of both constraint Jacobians can be exploited to efficiently solve the resulting equation systems, but the reduced model even further reduces the computational effort.

5. Time-optimal path following considering constraint forces

5.1. Optimization problem

For serial robots the joint velocities $\dot{\mathbf{q}}$, accelerations $\ddot{\mathbf{q}}$, possibly jerks $\dddot{\mathbf{q}}$ and the actuation torques $\boldsymbol{\tau}$, but no constraint forces λ are taken into account for time-optimal motion planning [50–52]. So far, this approach was adopted for parallel robots [53–59] where only the actuation torques $\boldsymbol{\tau}$ are limited. However, consideration of constraint forces for time optimal motion planning was already presented by [60] in 1992 but not applied later.

For the time-optimal path following problem the desired geometric path of the EE $\mathbf{z}(s)$ is described using a path parameter $s \in [0, 1], \dot{s} \geq 0$. The time derivative \dot{s} determines how fast the trajectory progresses along this specified path and is directly related to the time t . This gives rise to the optimization problem

$$\min_{\dot{s}} t_e = \min_{\dot{s}} \left(\int_0^1 \frac{1}{\dot{s}} ds \right) \quad (33)$$

$$\text{s.t. } 0 < s < 1, \dot{s} > 0, \dot{s}(0) = 0, \dot{s}(1) = 0, \quad (34)$$

$$\dot{\mathbf{q}}_{\min} \leq \dot{\mathbf{q}} \leq \dot{\mathbf{q}}_{\max}, \ddot{\mathbf{q}}_{\min} \leq \ddot{\mathbf{q}} \leq \ddot{\mathbf{q}}_{\max}, \quad (35)$$

$$\ddot{\mathbf{q}}_{\min} \leq \ddot{\mathbf{q}} \leq \ddot{\mathbf{q}}_{\max}, \quad (36)$$

$$\tau_{\min} \leq \tau \leq \tau_{\max}, \lambda_{\min} \leq \lambda \leq \lambda_{\max} \quad (37)$$

for a time-optimal motion, where t_e denotes the terminal time. The upper and lower limit of the torques τ and constraint forces λ are indicated with $(\cdot)_{\max}$ and $(\cdot)_{\min}$. From the inverse kinematics the joint angles \mathbf{q} and derivatives w.r.t. the path parameter $\mathbf{q}', \mathbf{q}''$ are obtained as functions of $\mathbf{z}, \mathbf{z}', \mathbf{z}''$, where $(\cdot)'$ denotes the derivative w.r.t. s . This yields the relations [61]

$$\dot{\mathbf{q}} = \mathbf{q}' \dot{s}, \quad (38)$$

$$\ddot{\mathbf{q}} = \mathbf{q}'' \dot{s}^2 + \mathbf{q}' \ddot{s}, \quad (39)$$

$$\ddot{\mathbf{q}} = \mathbf{q}''' \dot{s}^3 + \mathbf{q}'' 3\dot{s}\ddot{s} + \mathbf{q}' \ddot{\ddot{s}}. \quad (40)$$

Inserted in the inverse dynamics model (1) yields the actuation torques

$$\tau = \mathbf{A}_\tau \ddot{\mathbf{s}} + \mathbf{B}_\tau \dot{s}^2 + \mathbf{C}_\tau + \mathbf{D}_\tau \dot{s}. \quad (41)$$

Analogously, the constraint forces are expressed as

$$\lambda = \mathbf{A}_\lambda \ddot{\mathbf{s}} + \mathbf{B}_\lambda \dot{s}^2 + \mathbf{C}_\lambda + \mathbf{D}_\lambda \dot{s}. \quad (42)$$

This computation of constraint forces is the crucial part that requires physically consistent dynamics parameters.

There are various ways to solve (33). One approach is to introduce the variable $z = (\dot{s})^2$ to simplify the optimization. When looking for the scalar function of the path parameter s , dynamic programming [62, 63] can be applied. Sequential convex programming [64] using slack variables provides another but computationally expensive method. A computationally less demanding approach to solve this optimization is to use the parameter linear reformulation presented in [65]. Therein, a B-Spline is used to represent the squared path speed z and the cost function (33) is changed to

$$\max_{z(s)} \left(\int_0^1 z(s) ds \right) \quad (43)$$

$$\text{s.t. (34)–(37).} \quad (44)$$

The latter approach was used to solve the time-optimal path following problem under consideration of the convex (35) and non-convex constraints (36), (37). The idea behind the new cost function in (43) is to maximize the squared path speed $z(s)$ along the trajectory to obtain time-optimal solution for the given path. This eliminates the singularities at the start and end of the path, when the path speed is zero. The formulation (43), (34)–(37) is used in the following.

5.2. Post-processing of optimized trajectory

The result of the optimization (43) is the squared path speed $z(s)$ over the chosen discretization of s . Due to the non-linear relation

$$t(s) = \int_0^s \frac{1}{\sqrt{z(\sigma)}} d\sigma \quad (45)$$

a non equidistantly distributed time vector is the result. For evaluating this integral at the start $s = 0$ and end $s = 1$ of the path parameter, where $z(s) = 0$, the reader is referred to [63]. For the actual real-time control the optimized trajectory is required as a function of time t and not of the path parameter s . We recommend storing the optimized trajectory as a look-up table over time on the control unit. A non-uniform time sampling can be used for the implementation on the real-time system, but comes at the price of a computationally expensive online (spline) interpolation for $\mathbf{q}, \dot{\mathbf{q}}, \ddot{\mathbf{q}}$ or $\mathbf{z}, \dot{\mathbf{z}}, \ddot{\mathbf{z}}$. This interpolation can violate the real-time condition that all necessary computations must be finished within the sampling time T_S . This violation depends on the used CPU and the set sampling time. Violation of the real-time condition in turn leads to an emergency stop and shutdown. For our setup, as later explained in Section 6.1, these emergency stops were

observed when using the expensive spline interpolation. To keep the computational effort of the control unit as low as possible, we recommend storing the optimized trajectory using the sampling time T_S as discretization for the look-up table. To avoid even a linear interpolation of the desired trajectory on the real time system, the closest point search method can be used.

Based on the chosen discretization for the path parameter s the relation (45) has to be evaluated yielding the corresponding time values $t_i(s_i)$. To obtain the path parameter values $s_i(t_i)$ with the system tick as time discretization the inverse mapping is required. However, this inverse mapping $s(t)$ is only numerically available. The function $t(s)$ is a strictly monotonically increasing and guarantees the existence of the inverse function. According to the obtained non-equidistantly distributed path parameter samples $s_i(t_i)$ the desired task space trajectory $\mathbf{z}, \dot{\mathbf{z}}, \ddot{\mathbf{z}}$ or joint trajectory $\mathbf{q}, \dot{\mathbf{q}}, \ddot{\mathbf{q}}$ is reconstructed (38)–(40) and stored in a look-up table with the time t_i as input variable.

6. ABB robot IRB 360-6/1600

6.1. Experiment setup and data filtering

An Automation PC 5PC910.SX02-00 with an Intel Core i7 6820EQ CPU from Bernecker and Reiner Industrial Automation (B&R) is used to control the motion task at a cycle time of 400 μ s. Two ACOPOS P3 servo amplifier 8EI8X8MWT10 control the motors equipped with 15 bit absolute encoders.

The regressor matrix $\mathbf{Y}(\mathbf{q}, \dot{\mathbf{q}}, \ddot{\mathbf{q}})$ is a function of the (joint) angles, velocities and accelerations. For a standard industrial robot the only measurable quantities are the joint angles \mathbf{q} . Numerical differentiation is required to compute the joint velocities and accelerations. Depending on the quality of the position measurement different approaches can be used. According to [47] a Discrete Fourier Transformation (DFT) can be used to obtain numerical values for $\dot{\mathbf{q}}$ and $\ddot{\mathbf{q}}$. Another approach is to use the (central) difference quotient for the joint velocities and accelerations, but this requires a high quality position measurement, since the effect of noise is amplified by every numerical differentiation.

In this paper, a forward difference quotient was used to obtain the joint velocities $\dot{\mathbf{q}}$ and the Matlab function *filtfilt* [66] with a differentiation filter for the joint accelerations $\ddot{\mathbf{q}}$. The *filtfilt* command further cancels the effect of group delay by forward and backward differentiation of the joint angles. A necessary precondition for this approach is the existence of a high quality encoder, this is met by our experiment setup. Due to the high quality absolute encoders, no (pre)filtering of the measured joint angles with a low-pass filter was necessary.

6.2. Identification of the disassembled robot

In a first step for the identification process the telescope bar, struts, and the platform are removed, as seen in Fig. 7. The robot now only consists of the three actuated upper arms and the drive for the telescope bar. This approach allows an independent rigid body parameter identification of the upper arms with their drive unit and the motor for the telescope bar. Optimized Fourier trajectories serve as persistent excitation trajectories for the identification of both the disassembled and assembled PKM. These results are used as regularization/initial values of the upper arms and friction coefficients for the identification of the assembled robot in Section 6.3. Disassembling the robot further allows reducing the uncertainties and eliminates the effect of friction appearing in passive joints.

6.2.1. Covariance matrix of torque measurement

The disassembled state of the robot can be used to easily obtain an estimate of the covariance matrix of the motor torque measurement.



Fig. 7. Picture of the disassembled Delta robot. This setup is used for the identification of the upper arms and rotatory inertia of motor four driving the telescope bar.

In estimation theory [44] it is common practice to assume an additive Gaussian noise model for the measurement error. To this end, different additional weights (1 kg and 2.5 kg) were mounted on the upper arms and different static poses recorded. The formulae $\hat{\mu} = 1/N \sum_{i=1}^N x_i$ and $\hat{\sigma}^2 = 1/(N-1) \sum_{i=1}^N (x_i - \hat{\mu})^2$ for obtaining the mean value and an estimate of the variance [43] are applied to the motor torque samples x_i of each axis and for each pose. It was observed that the variance of the motor torque measurement $\hat{\sigma}^2$ slightly decreased with an increasing mean value of the motor torque, but is still within the same decimal power. Since the IRB 360 is intended to handle loads up to 6 kg, the computed variance for the 2.5 kg test weight was used for the torque measurement of the ACOPOS Servo Drives. For the actuation torques τ in the EOM (1) the motor torques are multiplied with the gear ratio i_G . The estimate of the variance $\hat{\sigma}^2$ for the motor torques has to be multiplied with the squared gear ratio i_G^2 , according to the multiplication rules of random variables [44], to obtain the variances $\hat{\sigma}_\tau^2 = \hat{\sigma}^2 i_G^2$ of the generalized actuation torque τ . These four variances are the main diagonal elements of the estimated covariance matrix $\hat{\Sigma}$. The proposed approach to estimate the variance of the generalized torque measurement is also applicable to any assembled robot, regardless if it is a PKM or a serial robot.

6.2.2. Base-parameter identification of upper arms and drive of the telescope bar

The base-parameters for each of the three upper arms including their drive units are

$$\mathbf{p}_{B,UA} = [m c_x \quad m c_z \quad \Theta_{yy} \quad p_v \quad p_C]^T. \quad (46)$$

For the drive of the telescope bar

$$\mathbf{p}_{B,TB} = [\Theta \quad p_v \quad p_C]^T \quad (47)$$

only the lumped rotatory inertia Θ together with the two friction coefficients contribute to the EOM. Direct use of the weighted LS solution (9) with \mathbf{W}_τ or Σ^{-1} , for the base-parameters yields the results shown in Table 1. Therein, $C_M i_G^2$ denotes the lumped inertia of the fourth motor w.r.t. the gear box output. The difference of the two parameters obtained by the different weighting matrices is in the order of 10^{-13} , which is the numerical tolerance. Usage of the in Section 6.2.1 proposed covariance matrix Σ as well as the maximal motor torques $\text{diag}(\tau_{\max})$ as weighting matrix \mathbf{W}_τ yielded the same results. For the three upper arms the inertia parameters achieved alike results. This justifies the simplification applied in Section 6.3.3, that it is sufficient to use one set of inertia parameters for the upper arms instead of three slightly different ones. The values of the viscous and Coulomb friction coefficients of the first three drives (upper arms) are also roughly in the same numerical region. The friction values of the drive for the telescope bar are noticeably smaller than the other ones. Fig. 8 show the verification of the separate identification of the reduced system.

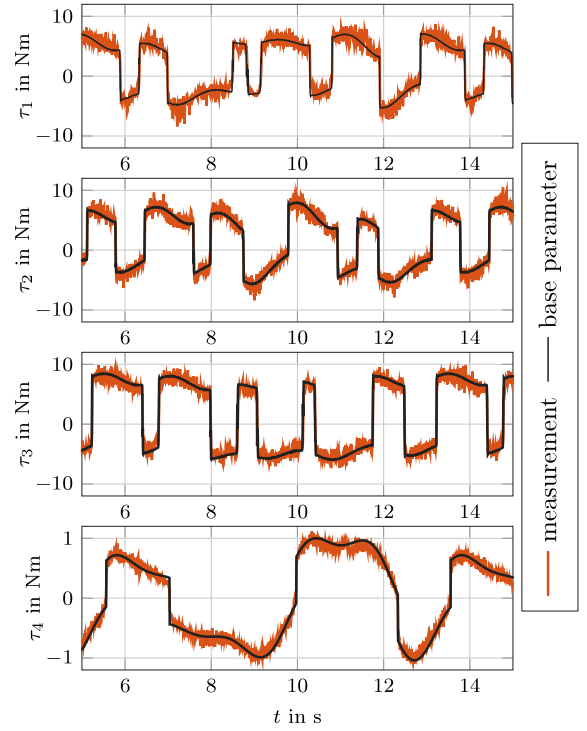


Fig. 8. Verification of the base-parameter identification of the disassembled robot.

Table 1

Results of base parameter identification of upper arms and drive of the telescope bar.

	Arm 1	Arm 2	Arm 3	Drive 4	Unit
$m c_x$	0.150	0.153	0.152		kg m
$m c_z$	0.005	0.007	0.016		kg m
Θ_{yy}	0.228	0.232	0.238		kg m ²
p_C	4.201	4.145	5.773	0.387	Nm
p_v	0.281	0.419	0.448	0.012	$\frac{\text{Nm}}{\text{rad/s}}$
$C_M i_G^2$				0.003	kg m ²

6.3. Identification of the assembled robot

6.3.1. Identification of the non-linear friction model for drive 4 with the telescope bar

There are no limits on the rotation angle of the fourth motor driving the telescope bar. The maximal motor speed is 3200°/s at the gear box output. Based on previous results of the friction identification in [38] the friction model considering Coulomb and linear viscous friction is insufficient to account for the large speed range $\dot{q}_4 \in [-3200^\circ/\text{s}, 3200^\circ/\text{s}]$, as seen in Fig. 9. For a constant velocity, the occurring motor torque only compensates the friction, regardless of the driven inertia [67]. To obtain the friction curve (motor torque over joint speed), the motor torque and motor speed are measured and averaged for a constant velocity. This yields one discrete point of the friction curve. To obtain more points on the friction curve, this process is repeated for various speeds in both positive and negative direction. However, this approach can only be applied to the telescope axis since the other drives actuating the upper arms cannot perform continuous rotation. Fig. 9 shows the resulting friction curve. A non-linear, but almost symmetric curve with a saturation occurring already at a third of the maximal speed is obtained. Since the nominal motor torque of the fourth motor is by far not reached, the motor is definitely not in any magnetic saturation. A symmetric model for the friction torque

$$\tau_{4,f} = A_C \tanh(100 \dot{q}_4) + A_v \tanh\left(\frac{\dot{q}_4}{\epsilon_v}\right) \quad (48)$$

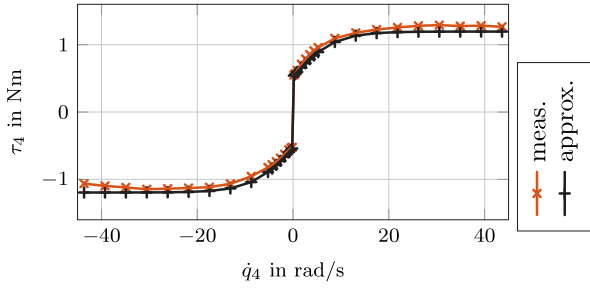


Fig. 9. Curve of the friction torque of the fourth motor of the IRB 360.

Table 2

Identified friction coefficients for the non-linear friction model (48) of the motor driving the telescope bar. The gear ratio is considered in these values.

	Drive 4	Unit
A_c	0.5272	Nm
A_v	0.6672	Nm
ϵ_v	8.5919	rad/s

is used as approximation with parameters A_c for the Coulomb friction, and A_v with ϵ_v for the velocity dependent part. A non-linear least squares curve fitting was used to identify these parameters, the results are stated in Table 2.

6.3.2. Regularization values

The results of the separate base-parameter identification of the upper arms in Section 6.2.2 are used as regularization for the inertia parameters of the upper arms as well as the viscous and Coulomb friction coefficients of the drives.

The manufacturers CAD data for the IRB 360 does not contain any volumetric information and is hence not suited to compute mass moments. Disassembling the mechanism yields an advantageous opportunity to measure and weigh parts of the robot and compute regularization values p_{reg} as proposed in Section 3.3.

The slender struts are $L = 1106$ mm long, the measured outer radius is $R = 8$ mm, the inner radius $r = 7$ mm is assumed, and the weight $m_S = 0.150$ kg is measured. Assuming the COM to be in the geometric center yields the regularization value for the struts. The weight of the platform $m_P = 1.12$ kg was measured. The platform of the Delta robot only performs linear (translational) motions, hence only the mass of the platform contributes to the EOM. The telescope bar consists of an upper and lower part, connected by a prismatic joint. This prismatic joint has an end stop, which does not allow a further disassembling. The weight of both parts is $m_{TB} = 1.14$ kg. The upper part is assumed as a cylinder with $m_{TU} = \frac{6}{10} m_{TB}$ with length $L = 760$ mm and radius $r = 6$ mm, the COM to be in the middle of the center line. The lower part is approximated as hollow cylinder with mass $m_{TL} = \frac{4}{10} m_{TB}$, length $L = 800$ mm, inner and outer radii $r_i = 6$ mm and $r_o = 16$ mm, respectively. Again, the COM is assumed in the geometric center.

6.3.3. Identification results

With the previously described simplifications and assumptions only 18 transformed optimization variables are necessary for describing the required inertia, 8 variables for the linear friction model of the first three axes and the prismatic joint of the telescope bar, and 3 variables for the non-linear friction model. This results in only 29 optimization variables, whereas the base-parameter approach (which does not account for the non-linear friction model) has 37 parameters, see [38] for more details. Without the mentioned assumptions and simplifications 51 optimization variables would be necessary for the rigid body inertia parameters. The identification results are summarized in Table 3 for the rigid bodies and in Table 4 for the friction. The result for the upper arms did not change much w.r.t. to Section 6.2.2. Due to the limited

Table 3

Identified rigid body inertia for the Delta robot ABB IRB 360-6/1600.

Parameter	Value	Unit
Strut		
m	0.179	kg
$m c_x$	0.076	kg m
Θ_{xx}	1.50E-05	kg m ²
Θ_{yy}	0.075	kg m ²
Θ_{zz}	0.075	kg m ²
Arm		
$m c_x$	0.176	kg m
$m c_z$	0.006	kg m
Θ_{yy}	0.258	kg m ²
Platform		
m	1.200	kg
Telescope bar (upper part)		
m	0.922	kg
$m c_z$	-0.219	kg m
Θ_{xx}	0.084	kg m ²
Θ_{yy}	0.084	kg m ²
Θ_{zz}	1.90E-05	kg m ²
Telescope bar (lower part)		
m	0.557	kg
$m c_z$	0.146	kg m
Θ_{xx}	0.077	kg m ²
Θ_{yy}	0.077	kg m ²
Θ_{zz}	3.00E-05	kg m ²

Table 4

Identified friction coefficients of the first three drive units and the prismatic joint connecting upper and lower part of the telescope bar. The prismatic joint is abbreviated with P-TB.

	Drive 1	Drive 2	Drive 3	P-TB	Unit
p_C	4.667	4.376	6.466	1.641	Nm
p_v	1.727	2.064	1.557	1.247	$\frac{\text{Nm}}{\text{rad/s}}$

motion possibilities of the telescope bar, the result of the identification was basically the initial guess. The lower part of the telescope bar can perform more dynamic motions and the result slightly differed from the regularization term.

The viscous coefficients of the drives more than tripled relative to the base-parameter result in Section 6.2.2. This increase can only be explained by further (not modeled) friction in other joints. The additional friction is captured by increased viscous friction of the drives. Investigating the real robot shows that there is a significant friction in the ball sockets of the spherical joints. This can only be observed when the telescope bar and two of the three limbs are dismounted. Friction in the passive joints is accounted for by the increased friction coefficients of the actuated joints and the ones directly proportional to the platform velocity. Modeling friction in passive joints would lead to an increase of optimization variables. In case of the Delta, 12 additional viscous and Coulomb friction coefficients would be needed, resulting in a larger model. To keep the model as simple as possible to evaluate it on the real-time control system, this effect is not further investigated.

6.4. Inverse dynamics verification

To verify the identified parameters a different excitation (Fourier) trajectory is executed, recorded, and the measured torques compared to the computed ones based on the identification. Fig. 10 shows the results of the verification. The actuation torques computed using the base-parameters and the proposed identification yield similar results. For the fourth axis (driving the telescope bar) the physically consistent identification with the non-linear friction model yielded a smoother result as can be seen in the last plot of Fig. 10 for τ_4 between 6 s and 7 s and 11 s and 12 s.

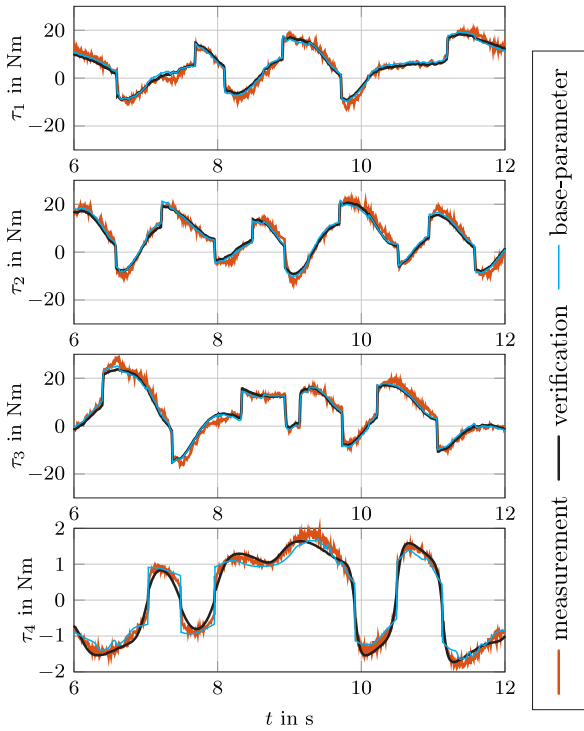


Fig. 10. Actuation torques τ for the verification trajectory. A root mean squared error $e_{\text{rms}} = [1.5 \ 1.5 \ 1.6 \ 0.17] \text{ Nm}$ is obtained for the base-parameters, whereas the proposed identification yields $e_{\text{rms}} = [1.5 \ 1.6 \ 1.7 \ 0.16] \text{ Nm}$.

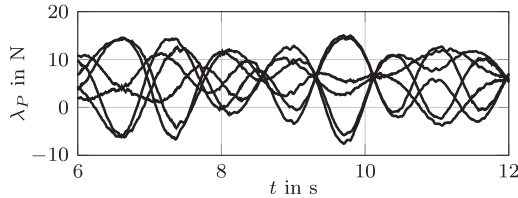


Fig. 11. Computed longitudinal strut forces $\lambda_{P,i}, i = 1 \dots 6$ for the verification trajectory.

The obtained inverse dynamics solution fit well, but this does not necessarily mean that the computed strut force is correct. Fig. 11 shows the calculated strut forces $\lambda_{P,i}$ for the considered verification trajectory without any additional load on the EE. The strut forces are plausible, since the platform weighs about 1 kg and the forces are within the range from roughly -10 N to about 15 N .

6.5. Strut force verification

To measure an internal force of the mechanism, one of the original struts was replaced. Because the ball socket joint (see Fig. 1) is realized by means of a clamped spring, it can be disassembled. This was exploited for measuring the longitudinal force in the strut. To this end, a measurement strut was designed comprising a force sensor. A carbon fiber tube with an outer diameter of 16 mm is used as starting point to replace one of the original struts. A standard ball socket is glued to one end of the strut and additionally fixed with a pin, such that the original spring clamps still work. At the other end of the tube two cylindrical adapters with are used to fix the force sensor KM26z, as seen in Fig. 12, such that the final length of the strut can be adapted and fit into the assembled robot. To minimize interference also a light force sensor is used. The self build measurement strut weighs 340 g, roughly twice as much as the identified strut mass. This sensor can only measure longitudinal forces and does not tolerate lateral forces or torques. The

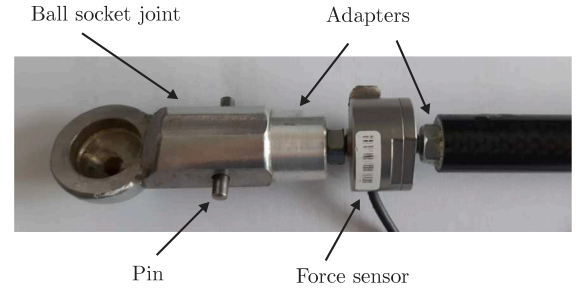


Fig. 12. Upper end of the measurement strut with the force sensor.

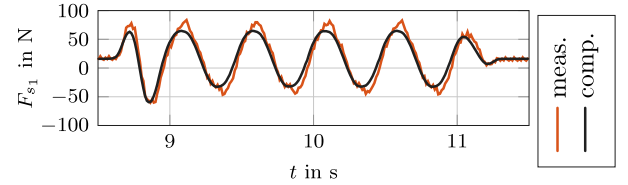


Fig. 13. Measurement (meas) and computation (comp) of the longitudinal force F_{S1} at the upper end of the first strut based on the conducted identification and an additional 5 kg weight plate.

struts are slightly bent due to the spring clamps, which causes a bending moment on the force sensor. Two spacers are used to straighten the two struts of the parallelogram where the measurement strut is installed to ensure only longitudinal loads on the sensor. As a consequence, only up and down motions along the center line of the Delta are possible in this setup.

Fig. 13 shows the measured and computed strut force for an up and down motion of the EE using an additional 5 kg weight plate. This additional weight is required to achieve higher strut forces. The measurement and computation fit well.

6.6. Optimized pick and place trajectory

The geometric path of a typical pick and place task of a Delta robot is described using B-splines. It is a planar, symmetric motion along the y -axis of the inertial frame \mathcal{F}_I with a length of 800 mm and height of 180 mm. The path is depicted in Fig. 14. Typically, a 90° rotation of the EE is part of the motion. However, this rotation is omitted due to the additional laser tracker measurement, the laser tracker eye would be out of scope. A 2.5 kg dumbbell weight plate is used as load on the EE. The optimization for the time-optimal motion obtained from (43), uses the previously identified dynamics parameters. The limits for the first three actuated joints are $\dot{q}_{\text{max}} = 1088^\circ/\text{s}$, $\ddot{q}_{\text{max}} = 5000^\circ/\text{s}^2$, $\ddot{q}_{\text{max}} = 100000^\circ/\text{s}^3$. The limits for the motor torques and speeds are set according to the available data sheet, whereas the limits for the motor accelerations and jerks are up to the user. The computed constraint forces λ comprise the actuation torques τ as λ_A , as shown in Section 4. The chosen limits for the constraint forces are $\bar{\lambda}_A = 4 \text{ Nm}$, $\bar{\lambda}_{E,j} = 10 \text{ Nm}, j = 1, 2$, $\bar{\lambda}_{E,j} = 140 \text{ N}, j = 3, 4, 5$ and $\bar{\lambda}_S = 120 \text{ N}$. A 10% safety margin for the limitation of torques and forces is considered to protect the mechanics and drives. For simplicity, the strut forces λ_P occurring between the platform and the struts are omitted.

Fig. 15 shows the maximum velocity curve (MVC) [68] together with the optimal squared path speed $z_{\text{opt}}(s)$ for the U-turn. The two valleys at $s = 0.2$ and $s = 0.8$ correspond to the rounded corners of the motion at which the squared path speed z attains the MVC. These two parts of the motion are the most restrictive segments of the path. The optimized motion takes $\approx 0.48 \text{ s}$. Fig. 16 shows the planned strut forces during the time-optimal motion, where the limitation can clearly be seen. During the execution of the straight line of the U-turn the strut

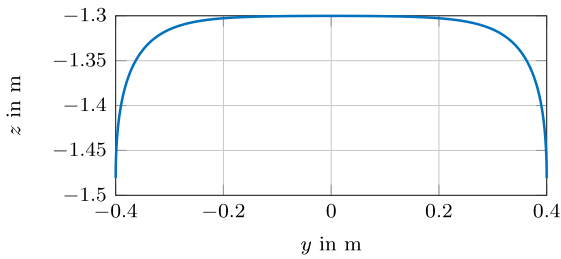


Fig. 14. Path of the optimized U-turn motion.

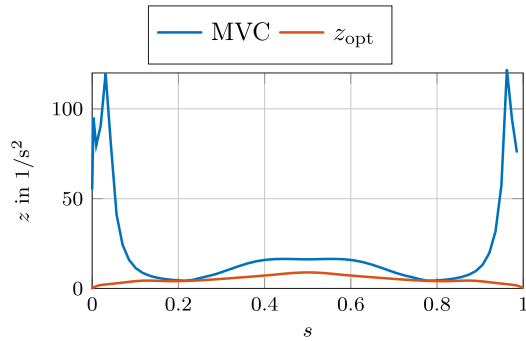


Fig. 15. Maximum velocity curve and optimal squared path speed z of the optimized U-turn motion.

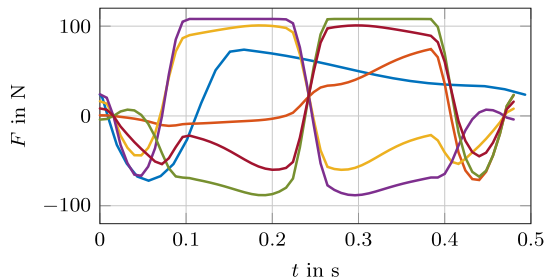


Fig. 16. Computed strut forces for the optimized U-turn motion.

forces are the limitation of the motion rather than the joint torques. The laser tracker measurement was differentiated using the Matlab command *filtfilt*. The results of the EE acceleration are presented in Fig. 17, the measured and planned EE acceleration fit well. Matlab with Yalmip [69] using *fmincon* was used to solve the optimization problems (10) and (43).

7. Conclusion

Physical consistency is vital for forward dynamics simulation, application of model-based control schemes and the computation of constraint forces. Especially the latter require physical consistency of the 10 inertia parameters of all rigid bodies comprised in the multi-body system model. No robot manufacturer provides sufficient CAD data to obtain estimates for the inertia parameters.

Disassembling the robot would be in ideal approach to obtain inertia parameters, but unfortunately this is not possible. However, Delta-like robots can partially be disassembled while still being functional. Disassembling the Delta allows measuring the weight of the bodies and yields good estimated inertia values. Identification of the disassembled manipulator further revealed the effect of unmodeled friction of the passive joints, an increase of the viscous friction coefficients of the active joints is the result. Exploiting the parallel structure in combination with certain model assumptions on the COM and inertia allowed to

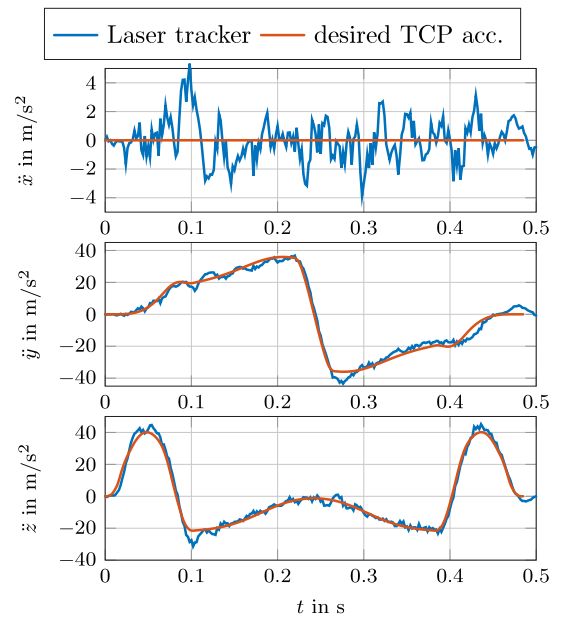


Fig. 17. Measured and computed EE acceleration for an optimized motion.

systematically reduce the required number of optimization variables, speed up the computation, and improve the identification result. The identified dynamics parameters are summarized in Tables 2, 3, and 4 to provide a reliable dynamics model of the ABB IRB 360-6/1600 for the robotics community.

The longitudinal strut forces have been identified as a vital constraint force appearing in the mechanism of Delta-like robots [39]. To incorporate selected constraint forces in the motion planning a reduced model, less complex than an absolute coordinate model, is proposed. This model was verified with a measurement strut including a force sensor. A typical pick and place task is considered demonstrating the proposed model for time-optimal motion planning. This method is generally applicable for various parallel robots belonging to the class of Delta-like robots. Limitation of both constraint forces and actuation torques is crucial to expand the lifetime of a robot and save maintenance costs.

Future work will investigate the effect of friction occurring in passive joints, such as the discussed ball socket joints or the prismatic joint of the telescope bar. The friction occurring in the telescope bar, especially when the two parts quickly retract, should be investigated. Furthermore, modeling elasticities will be the next step for the PKM.

CRediT authorship contribution statement

Daniel Gnad: Writing – review & editing, Writing – original draft, Validation, Software, Methodology, Investigation. **Hubert Gattringer:** Supervision, Writing – review & editing. **Andreas Müller:** Writing – review & editing, Supervision. **Wolfgang Höbarth:** Resources. **Roland Riepl:** Resources. **Lukas Meßner:** Resources.

Declaration of competing interest

The authors declare that they have no known competing financial interests or personal relationships that could have appeared to influence the work reported in this paper.

Data availability

The data that has been used is confidential.

Acknowledgments

This work has been supported by the LCM K2 Center for Symbiotic Mechatronics within the framework of the Austrian COMET-K2 program.

References

- [1] C.D. Sousa, R. Cortesão, Physically feasible dynamic parameter identification of the 7-DOF WAM robot, in: *IEEE/RSJ Int. Conf. Intell. Rob. Sys.*, 2013, pp. 2868–2873.
- [2] H. Khalil, *Nonlinear Systems*, Prentice-Hall, 2002.
- [3] R. Ortega, E. García-Canseco, Interconnection and damping assignment passivity-based control: A survey, *Eur. J. Control* 10 (5) (2004) 432–450.
- [4] R. Kelly, R. Carelli, A class of nonlinear PD-type controllers for robot manipulators, *J. Robot. Syst.* 13 (12) (1996) 793–802.
- [5] P. Nikravesh, *Computer-Aided Analysis of Mechanical Systems*, Prentice-Hall, 1988.
- [6] A.A. Shabana, *Dynamics of Multibody Systems*, Cambridge University Press, 2020.
- [7] W. Khalil, E. Dombre, *Modeling, Identification and Control of Robots*, Butterworth-Heinemann, 2004.
- [8] K. Yoshida, K. Osuka, H. Mayeda, T. Ono, When is the set of base-parameter values physically impossible? *J. Robot. Soc. Jpn.* 14 (1) (1996) 122–130.
- [9] K. Yoshida, W. Khalil, Verification of the positive definiteness of the inertial matrix of manipulators using base inertial parameters, *Int. J. Robot. Res.* 19 (5) (2000) 498–510.
- [10] C.D. Sousa, R. Cortesão, Physical feasibility of robot base inertial parameter identification: A linear matrix inequality approach, *Int. J. Robot. Res.* 33 (6) (2014) 931–944.
- [11] S. Traversaro, S. Brossette, A. Escande, F. Nori, Identification of fully physical consistent inertial parameters using optimization on manifolds, in: *IEEE/RSJ Int. Conf. Intell. Rob. Sys.*, 2016, pp. 5446–5451.
- [12] C.D. Sousa, R. Cortesão, Inertia tensor properties in robot dynamics identification: A linear matrix inequality approach, *IEEE/ASME Trans. Mechatronics* 24 (1) (2019) 406–411.
- [13] P.M. Wensing, S. Kim, J.-J. Slotine, Linear matrix inequalities for physically-consistent inertial parameter identification: A statistical perspective on the mass distribution, *IEEE Robot. Autom. Lett.* 3 (1) (2018) 60–67.
- [14] C. Gaz, M. Cognetti, A. Oliva, P. Robuffo Giordano, A. De Luca, Dynamic identification of the franka emika panda robot with retrieval of feasible parameters using penalty-based optimization, *IEEE Robot. Autom. Lett.* 4 (4) (2019) 4147–4154.
- [15] T. Lee, P.M. Wensing, F.C. Park, Geometric robot dynamic identification: A convex programming approach, *IEEE Trans. Robot.* 36 (2) (2020) 348–365.
- [16] T. Lee, F.C. Park, A geometric algorithm for robust multibody inertial parameter identification, *IEEE Robot. Autom. Lett.* 3 (3) (2018) 2455–2462.
- [17] C. Rucker, P.M. Wensing, Smooth parameterization of rigid-body inertia, *IEEE Robot. Autom. Lett.* 7 (2) (2022) 2771–2778.
- [18] J.-P. Merlet, *Parallel Robots*, Springer-Verlag GmbH, 2005.
- [19] J.M.E. Hernandez, A. Chemori, H.A. Sierra, *Modeling and Nonlinear Robust Control of Delta-Like Parallel Kinematic Manipulators*, Elsevier, 2022.
- [20] R. Clavel, Delta, a fast robot with parallel geometry, in: *18th Int. Symp. Industrial Robots*, 1988, pp. 91–100.
- [21] F. Pierrot, O. Company, H4: a new family of 4-DOF parallel robots, in: *IEEE/ASME Int. Conf. Adv. Intell. Mechat.*, 1999, pp. 508–513.
- [22] F. Pierrot, F. Marquet, O. Company, T. Gil, H4 parallel robot: Modeling, design and preliminary experiments, in: *IEEE Int. Conf. Robot. Autom.*, Vol. 4, IEEE, 2001, pp. 3256–3261.
- [23] C. Baradat, V. Nabat, S. Krut, F. Pierrot, et al., Par2: A spatial mechanism for fast planar, 2-dof, pick-and-place applications, in: *Fundamental Issues and Future Research Directions for Parallel Mechanisms and Manipulators*, 2009, p. 10.
- [24] V. Nabat, O. Company, F. Pierrot, P. Poignet, Dynamic modeling and identification of Par4, a very high speed parallel manipulator, in: *IEEE/RSJ Int. Conf. Intell. Rob. Sys.*, 2006, pp. 496–501.
- [25] L.R. Douat, I. Queinnee, G. Garcia, M. Michelin, F. Pierrot, Flexible model identification of the parallel robot par2, in: *IEEE/RSJ Int. Conf. Intell. Rob. Sys.*, IEEE, 2010, pp. 6175–6180.
- [26] S. Krut, M. Benoit, H. Ota, F. Pierrot, I4: A new parallel mechanism for scara motions, in: *IEEE Int. Conf. Rob. Autom.*, Vol. 2, 2003, pp. 1875–1880.
- [27] M. Díaz-Rodríguez, V. Mata, Á. Valera, Á. Page, A methodology for dynamic parameters identification of 3-DOF parallel robots in terms of relevant parameters, *Mech. Mach. Theory* 45 (9) (2010) 1337–1356.
- [28] F. Abed Azad, S. Ansari Rad, M.R. Hair Yazdi, M. Tale Masouleh, A. Kalthor, Dynamics analysis, offline-online tuning and identification of base inertia parameters for the 3-dof Delta parallel robot under insufficient excitations, *Meccanica* 57 (2) (2022) 473–506.
- [29] S. Briot, M. Gautier, Global identification of joint drive gains and dynamic parameters of parallel robots, *Multibody Syst. Dyn.* 33 (2015) 3–26.
- [30] S. Briot, S. Krut, M. Gautier, Dynamic parameter identification of over-actuated parallel robots, *J. Dyn. Syst. Meas. Control* 137 (11) (2015) 111002.
- [31] N. Farhat, V. Mata, A. Page, F. Valero, Identification of dynamic parameters of a 3-dof RPS parallel manipulator, *Mech. Mach. Theory* 43 (1) (2008) 1–17.
- [32] H. Abdellatif, B. Heimann, J. Kotlarski, On the robust dynamics identification of parallel manipulators: Methodology and experiments, in: *Parallel Manipulators, New Developments*, 2008, pp. 1–20.
- [33] H. Abdellatif, B. Heimann, O. Hornung, M. Grotjahn, Identification and appropriate parametrization of parallel robot dynamic models by using estimation statistical properties, in: *IEEE/RSJ Int. Conf. Intell. Rob. Sys.*, 2005, pp. 157–162.
- [34] H. Abdellatif, B. Heimann, C. Holz, Time-effective direct dynamics identification of parallel manipulators for model-based feedforward control, in: *IEEE/ASME Int. Conf. Advanced Intelligent Mechatronics*, 2005, pp. 777–782.
- [35] P. Renaud, A. Vivas, N. Andreff, P. Poignet, P. Martinet, F. Pierrot, O. Company, Kinematic and dynamic identification of parallel mechanisms, *Control Eng. Pract.* 14 (9) (2006) 1099–1109.
- [36] L. Angel, J. Viola, Parametric identification of a delta type parallel robot, in: *Colombian Conf. Rob. Autom.*, CCGA, IEEE, 2016, pp. 1–6.
- [37] H. Abdellatif, B. Heimann, M. Grotjahn, Statistical approach for bias-free identification of a parallel manipulator affected by large measurement noise, in: *IEEE Conf. on Decision and Control*, 2005, pp. 3357–3362.
- [38] D. Gnad, A. Müller, H. Gatringer, Dedicated dynamic parameter identification for Delta-like robots, *IEEE Robot. Autom. Lett.* 9 (5) (2024) 4393–4400.
- [39] D. Gnad, H. Gatringer, A. Müller, W. Höbarth, R. Riepl, L. Messner, Computation of dynamic joint reaction forces of PKM and its use for load-minimizing trajectory planning, in: *Int. Conf. Rob. Autom.*, IEEE, 2022, pp. 4848–4854.
- [40] A. Mueller, Implementation of a geometric constraint regularization for multibody system models, *Arch. Mech. Eng.* 61 (2) (2014) 365–383.
- [41] H. Bremer, *Elastic Multibody Dynamics*, Springer, 2008.
- [42] T. Lee, B.D. Lee, F.C. Park, Optimal excitation trajectories for mechanical systems identification, *Automatica* 131 (2021) 109773.
- [43] J.P. Norton, *An Introduction to Identification*, Academic Press, 1986.
- [44] S.M. Kay, *Fundamentals of Statistical Signal Processing, Volume I: Estimation Theory*, Pearson, 1993.
- [45] M. Gautier, P. Poignet, Extended Kalman filtering and weighted least squares dynamic identification of robot, *Control Eng. Pract.* 9 (12) (2001) 1361–1372.
- [46] J. Swevers, C. Ganseman, D.B. Tukul, J. De Schutter, H. Van Brussel, Optimal robot excitation and identification, *IEEE Trans. Robot. Autom.* 13 (5) (1997) 730–740.
- [47] J. Swevers, W. Verdonck, J. De Schutter, Dynamic model identification for industrial robots, *IEEE Control Syst. Mag.* 27 (5) (2007) 58–71.
- [48] Q. Leboutet, J. Roux, A. Janot, J.R. Guadarrama-Olvera, G. Cheng, Inertial parameter identification in robotics: A survey, *Appl. Sci.* 11 (9) (2021) 4303.
- [49] W. Blajer, Methods for constraint violation suppression in the numerical simulation of constrained multibody systems – a comparative study, *Comput. Methods Appl. Mech. Engrg.* 200 (13–16) (2011) 1568–1576.
- [50] J. Bobrow, S. Dubowsky, J. Gibson, Time-optimal control of robotic manipulators along specified paths, *Int. J. Robot. Res.* 4 (3) (1985) 3–17.
- [51] F.G. Flores, A. Kecskeméthy, Time-optimal path planning along specified trajectories, in: *Multibody System Dynamics, Robotics and Control*, Springer Vienna, 2012, pp. 1–16.
- [52] L. Messner, H. Gatringer, H. Bremer, Efficient online computation of smooth trajectories along geometric paths for robotic manipulators, in: *Multibody System Dynamics, Robotics and Control*, Springer Vienna, 2012, pp. 17–30.
- [53] T. Huang, P. Wang, J. Mei, X. Zhao, D. Chetwynd, Time minimum trajectory planning of a 2-DOF translational parallel robot for pick-and-place operations, *CIRP Ann.* 56 (1) (2007) 365–368.
- [54] S. Lu, B. Ding, Y. Li, Minimum-jerk trajectory planning pertaining to a translational 3-degree-of-freedom parallel manipulator through piecewise quintic polynomials interpolation, *Adv. Mech. Eng.* 12 (3) (2020).
- [55] A. Khouchi, L. Baron, M. Balazinski, A decoupled approach to optimal time energy trajectory planning of parallel kinematic machines, in: *CISM Courses and Lectures*, Springer Vienna, 2006, pp. 179–186.
- [56] Y. Liu, C. Wang, J. Li, L. Sun, Time-optimal trajectory generation of a fast-motion planar parallel manipulator, in: *IEEE/RSJ Int. Conf. Intell. Rob. Sys.*, 2006.
- [57] T. Su, L. Cheng, Y. Wang, X. Liang, J. Zheng, H. Zhang, Time-optimal trajectory planning for delta robot based on quintic pythagorean-hodograph curves, *IEEE Access* 6 (2018) 28530–28539.
- [58] I. Pietsch, M. Krefft, O. Becker, C. Bier, J. Hesselbach, How to reach the dynamic limits of parallel robots? An autonomous control approach, *IEEE Trans. Autom. Sci. Eng.* 2 (4) (2005) 369–380.
- [59] A. Khouchi, L. Baron, M. Balazinski, Constrained multi-objective trajectory planning of parallel kinematic machines, *Robot. Comput.-Integr. Manuf.* 25 (4–5) (2009) 756–769.
- [60] J. McCarthy, J. Bobrow, The number of saturated actuators and constraint forces during time-optimal movement of a general robotic system, *IEEE Trans. Robot. Autom.* 8 (3) (1992) 407–409.
- [61] L. Messner, H. Gatringer, H. Bremer, Generating speed, torque and jerk limited trajectories along specified geometric paths in realtime, in: *Biomechanics / 752: Robotics*, 2011.

- [62] R. Bellman, *Applied Dynamic Programming*, Princeton University Press, Princeton, N.J., 1962.
- [63] D. Kaserer, H. Gatttringer, A. Muller, Nearly optimal path following with jerk and torque rate limits using dynamic programming, *IEEE Trans. Robot.* 35 (2) (2019) 521–528.
- [64] F. Debrouwe, W. Van Loock, G. Pipeleers, Q.T. Dinh, M. Diehl, J. De Schutter, J. Swevers, Time-optimal path following for robots with convex–concave constraints using sequential convex programming, *IEEE Trans. Robot.* 29 (6) (2013) 1485–1495.
- [65] T. Marauli, H. Gatttringer, A. Müller, A parameter-linear formulation of the optimal path following problem for robotic manipulator, in: *International Conference on Robotics in Alpe-Adria Danube Region*, Springer, 2023, pp. 342–349.
- [66] Matlab – filtfilt. URL <https://www.mathworks.com/help/signal/ref/filtfilt.html>.
- [67] M. Grotjahn, B. Heimann, Determination of dynamic parameters of robots by base sensor measurements, *IFAC Proc. Vol.* 33 (27) (2000) 279–284.
- [68] F. Pfeiffer, R. Johanni, A concept for manipulator trajectory planning, *IEEE J. Robot. Autom.* 3 (2) (1987) 115–123.
- [69] J. Lofberg, Yalmip: A toolbox for modeling and optimization in matlab, in: *IEEE Int. Conf. Rob. Autom.*, 2004, pp. 284–289.



Daniel Gnad received a Dipl.-Ing. degree in Mechatronics from Johannes Kepler University Linz (JKU) in 2020 and is currently working as Ph.D. student. His research is focused on physically consistent dynamics parameter identification, frequency domain identification and optimal control of mechatronical systems.



Hubert Gatttringer received a Dipl.-Ing. degree in Mechatronics and the Dr. tech. (Ph.D.) degree in Technical Sciences from Johannes Kepler University Linz (JKU) in 2001 and 2006, respectively. In 2011 he became Associate Professor with the Institute of Robotics at JKU. His research is focused on modeling and control of flexible link/joint robotic systems and walking machines, optimal path planning, and kinematically redundant industrial robots.



Andreas Müller obtained diploma degrees in mathematics (1997), electrical engineering (1998), and mechanical engineering (2000), and a PhD in mechanics (2004). He received his habilitation in mechanics (2011) and is currently professor in robotics at the Johannes Kepler University, Linz, Austria. His current research interests include holistic modeling, model-based and optimal control of mechatronic systems, redundant robotic systems, parallel kinematic machines, biomechanics, and computational dynamics.